Energy Engineering

Tech Science Press

https://doi.org/10.32604/ee.2026.086009

ARTICLE

Uncertainty Quantification of Energy Extraction in a Process of Carbon Sequestration in Fractured Reservoirs: A Coupled Heat Transfer Phase Transport Study

Ali Bozorgpour[1] **and Behshad Koohbor**[2,*]

[1]Faculty of Civil and Environmental Engineering, Tarbiat Modares University, Tehran, Iran
[2]GeoRessources Laboratory, CNRS, Université de Lorraine, ENSG, Vandoeuvre-Lès-Nancy, France

*Corresponding Author: Behshad Koohbor. Email: behshad.koohbor@univ-lorraine.fr

Received: 22 May 2026; Accepted: 11 September 2026; Published: 12 November 2026

ABSTRACT: Injecting CO_2 into depleted oil and gas reservoirs is a cost-effective method for geological CO_2 sequestration as these reservoirs commonly possess proven capacity and sealing structures, and require lower exploration costs. The extracted brine can also be utilized for various thermal purposes. The presence of both natural and induced fractures in depleted oil and gas reservoirs can significantly impact their capacity for CO_2 sequestration and thermal exploitation. Accurate simulation of the multi-phase transport and heat transfer resulting from CO_2 injection requires a clear definition of properties for both the fracture and porous media. However, estimation of these properties, especially those of fractures, can be challenging and subject to significant uncertainty. This paper evaluates the extent to which uncertainty in fracture and matrix parameters affects simulated flow and transport results and the associated CO_2 sequestration and geothermal energy extraction metrics. This is done through Monte Carlo-based uncertainty propagation analysis and Sobol-based global sensitivity analysis. Polynomial chaos expansions are used to analyze continuous changes of response variables with variations in the input parameters within a reasonable computational time. The effect of uncertainty in fracture length, aperture and rotation angle, longitudinal and transverse dispersivity, reservoir permeability and anisotropy, and the van Genuchten-Mualem parameters are assessed. Based on the results, these parameters are ranked according to their influence on the mass of stored CO_2, reservoir heat loss, brine-based heat flux in the production well, and a measure of the CO_2 travel time.

KEYWORDS: Depleted oil reservoir; geological CO_2 sequestration; fractured reservoir; heat transfer; numerical simulation; Sobol' indices

1 Introduction

Geological CO_2 sequestration (GCS) is a promising approach to offset rising carbon dioxide levels in the atmosphere to mitigate global warming [1]. An economically attractive option for GCS is to inject CO_2 into depleted oil/gas reservoirs [2]. Such depleted reservoirs commonly possess proven capacity and sealing structures, requiring fewer exploration costs than many other formations, as they often already have significant exploration history [3]. Further cost-saving can be achieved using existing oil/gas production infrastructure and deep-drilled wells [4,5]. Many of the previously discovered oil and gas reservoirs in the world are now either depleted or at the tail-end of their production life [6], providing a substantial potential capacity for GCS [5,7]. In addition, a considerable percentage of these depleted oil/gas reservoirs have thermal energy production potentials and thermal energy can be extracted from the produced hot brine [8],

Copyright © 2027 The Authors. Published by Tech Science Press. This work is licensed under a Creative Commons Attribution 4.0 International License, which permits unrestricted use, distribution, and reproduction in any medium, provided the original work is properly cited.

and the reservoir can also be used for CO_2-circulated geothermal energy production after the end of the sequestration phase [3]. The latter is often referred to as a CO_2 plume geothermal system. This concept, generally referred to as CO_2 plume geothermal (CPG), has been explored through dedicated techno-economic and numerical studies of CO_2-based heat and electricity generation [9], safety- and cost-oriented reviews of CO_2 storage [10], applications to fault-bounded and heterogeneous geothermal reservoirs [11,12], well-scale CPG production optimization [13], and multistage-stimulated CO_2-EGS performance [14]; fractured CO_2-based geothermal reservoirs have also been modeled using coupled thermo-hydro-mechanical simulation combined with machine-learning surrogates [15]. Fault- and fracture-zone properties are similarly recognized as first-order controls on both containment and pressurization risk in carbonate and other reservoirs [16], while conceptual-model uncertainty [17], regional-scale storage workflows [18], dual-porosity representations of fractured storage reservoirs [19], cross-scale characterization of CO_2 capture and storage [20], and enhanced-oil-recovery practice in challenging carbonate settings [21] further motivate the fracture-focused treatment adopted here; related fractured-reservoir sequestration and trapping studies [22,23] round out this body of work.

It is estimated that more than half of the world`s conventional oil and gas is stored in naturally fractured reservoirs [24]. The Middle East, for example, is dominated by such reservoirs [25]. Oil and gas reservoirs may also become artificially fractured during their lifespan to enhance hydrocarbon recovery [26,27]. Depleted hydrocarbon reservoirs of this type have received little attention as potential candidates for GCS systems [28]. This is partly because natural or induced fractures in such reservoirs are commonly regarded primarily as a geomechanical and containment risk—raising concerns over induced seismicity, fault reactivation, and preferential CO_2 leakage pathways toward shallower formations—rather than as a resource to be characterized and exploited, and partly because the coupled multiphase-flow, heat-transfer and geomechanical behavior of fractured reservoirs is more complex to simulate than that of the more homogeneous saline aquifers that have received the bulk of attention in the GCS literature. This perceived risk must nonetheless be weighed against the practical advantages of depleted hydrocarbon reservoirs noted above (proven containment history, existing site characterization, and reusable infrastructure), and a more quantitative, physics-based understanding of how fractures affect both CO_2 containment and the exploitable geothermal resource is needed to support this risk-benefit assessment; the present study aims to contribute to that understanding [29]. The permeability provided by fractures is often several orders of magnitude higher than the primary permeability of the porous rock matrix, resulting in preferential flow paths for the invading fluid [30]. The high permeability of fractures may result in a fast flow of CO_2 without significant storage in the reservoir, which may lead to increased spatial spreading, escaping, and leaking of CO_2 [31]. Hence, fractures are generally regarded as potential escape routes for the injected CO_2, which can negatively impact the storage capacity of a specific reservoir [32]. Field- and laboratory-informed evaluations of CO_2 leakage through fracture zones [33] and of fault reactivation via fracture-network connectivity [34] reinforce this concern; complementary core-scale NMR studies of residual CO_2 trapping [35] and recent reviews of leakage-risk assessment, monitoring, and control across GCS sites [36] provide additional context for the risk-benefit framing adopted here. This fracture-leakage risk is not purely a mass-transport problem, however: because CO_2 injection also imposes a strong thermal perturbation on the reservoir (cold CO_2 displacing hot brine), the resulting thermal contraction and pressure changes can themselves affect fracture aperture, effective permeability and, in turn, the leakage risk, while the same fracture network that controls leakage also controls how much of the geothermal resource can be recovered. Despite this coupling, the impact of fractures on the coupled phase transport and heat transfer for GCS is not well studied, and existing risk assessments of fractured GCS systems rarely incorporate the thermal response explicitly, despite recent calls in the broader fractured-rock literature for more integrated treatments of coupled flow, heat and geomechanical processes.

One way to study this problem fast and economically justifiable as a preliminary study is through numerical modelling and global sensitivity analysis [37].

Numerical models have been applied to GCS across various formation types, spanning from carbonate reservoirs [38] to sedimentary aquifers [29]. More recently, embedded- and explicit-discrete-fracture formulations have been used to simulate coupled CO_2-EOR and storage in fractured shale and tight reservoirs [39–42], multiscale CO_2 hydrate and hydrate-cap storage [43,44], CO_2-N2 mixture dissolution with cross-diffusion effects in saturated porous media [45], and large-scale parallel compositional simulation of CO_2 storage [46], while coupled multigrid solvers have targeted the numerical stiffness introduced by fractured porous media more broadly [47]. Predictions made by these models are commonly affected by input parameters and structural uncertainties caused by data inadequacy, simplifying assumptions, and natural stochasticity [48,49]. Managing the resulting negative effects on model reliability has two interrelated tasks [50]: (1) uncertainty propagation analysis (UPA) to quantify model output uncertainties and (2) global sensitivity analysis (GSA) to gain insight into the most significant contributors of model output uncertainty [51]. The majority of studies on GCS modeling employ discrete model scenarios to analyze the impact of input variations on model outputs [52]. However fewer studies have addressed formal UPA and GSA for various types of CO_2 sequestration problems [53–55]. In these studies, UPA is commonly done through Monte Carlo simulations (MCSs) by directly incorporating the numerical model, or using data-driven surrogate models such as neural networks [56], polynomial chaos expansion (PCE) [57], and support vector machines [5] to reduce the computational time. More recent workflows further combine Bayesian-optimized machine-learning surrogates with Monte Carlo-based UPA and Sobol-based GSA for CO_2 storage prediction [58,59]. Uncertainty in the numerical/geological model itself has also been shown to be a significant contributor to prediction spread in field-scale CCS case studies [60]. The most used GSA measure in previous studies is the variance-based Sobol Sobol indices, largely because, unlike local or one-at-a-time sensitivity measures, Sobol indices decompose the output variance into contributions from individual parameters and their interactions without assuming linearity or monotonicity of the input-output relationship, which is essential for the strongly nonlinear, multiphase and thermally coupled response addressed here [53,61–63].

Some specific features of depleted oil/gas reservoirs have been less explored in the past GCS modeling studies. In the context of both UPA and GSA, uncertain input parameters of interest are mostly reservoir permeability [53,64–66], reservoir porosity [62,64,65], van Genuchten-Mualem (VGM) parameter [61], fracture/fault angle [67], and CO_2 injection rate [54,66,68]. The output quantities of interest (QoIs) are CO_2 saturation, pressure buildup at a particular time and location [53,61], net CO_2 storage rate [65], and CO_2 leakage rate [53,66,69]. Few studies have addressed small/moderate-scale closed-boundary systems [38], typical of depleted oil/gas reservoirs, in which the thermal capacity and the uncertainty analysis of the extracted brine at the same time as the uncertainty associated with the injected CO_2 (i.e., coupled CO_2 sequestration and heat transfer for thermal extraction of hot brine) in an explicitly fractured domain with a single or multiple considerable conduits existing in the domain.

Stochastic techno-economic analysis of CO_2-circulated geothermal energy production in closed reservoir systems has already been addressed by [3], including UPA and GSA of the coupled process. The present study builds directly on that framework but focuses specifically on the role of an explicit fracture: rather than treating the reservoir as an equivalent homogeneous medium, the fracture is represented geometrically (with its own length, aperture and orientation as uncertain parameters), and the GSA is used to rank fracture properties against matrix properties for each output metric. The novelty of the present work therefore lies not in the general UPA/GSA framework, which follows established practice, but in this explicit fracture-vs-matrix Sobol ranking for the coupled CO_2 sequestration and geothermal heat extraction problem in a

closed, depleted-reservoir setting. The objective of this paper is to systematically evaluate how uncertainty in fracture and matrix parameters affects simulated results of coupled phase transport (i.e., CO_2 sequestration) heat transfer (i.e., brine-based geothermal energy extraction) metrics in an explicitly fractured domain. PCE meta-models are developed and used to analyze continuous changes in the response variables with variations in the input parameters within a reasonable computational time. The structure of the paper is as follows: the GCS problem and the governing equations of the mathematical model used in its simulations are described, the UPA and GSA methodology is explained, the results of UPA and GSA are presented concerning each of the output metrics, and physical insight is provided. The paper is wrapped up with a summary of the key findings.

2 Methodology

2.1 Problem Statement and the Simulation Domain

Flow in a reservoir can be dominated by flow in a single fracture or fault [70–72], or by an interconnected network of fractures [73]. In both situations, the temporal and spatial characteristics of flow and heat exchange between the fluid flow in a single fracture and the surrounding rock matrix play a key role in reservoir performance [74]. Hence, in line with the purpose of this study, a simplified single-fracture closed-boundary system is assumed, as illustrated in Fig. 1a. The problem consists of a 500 m × 500 m × 150 m reservoir sector including a CO_2 injection well in one corner, and a production well at the opposite corner (i.e., diagonally) in a single explicitly fractured porous media. For the sake of simplicity and reducing the calculation effort, the solution domain is assumed only in the *x*-*y* plane, and the phase saturation and temperature in the *z*-direction are assumed constant (i.e., the dimension of the solution is reduced from three dimensions to two). Because the 2D domain represents a horizontal (*x*-*y*) slice of the reservoir, the gravity term ($\rho g \nabla z$) in Eq. (1) acts out of plane and is effectively absent from the simulated flow field; buoyancy-driven CO_2 override and vertical gravity segregation are therefore not captured. This is an acceptable simplification for the purpose of this preliminary, sensitivity-oriented study, which focuses on the horizontal, fracture-controlled component of plume migration, but it is a limitation that should be considered when extending the conclusions to full 3D reservoir behavior, where gravity override typically promotes upward CO_2 migration and can alter the sweep efficiency and the fracture-vs-matrix balance reported here. The simulation domain and boundary conditions, as well as the position of the injection and production wells, are illustrated in Fig. 1b. The porous matrix is homogeneous but anisotropic (i.e., with different permeability in the and directions). The fracture has an inclination angle of, length of, and an aperture of.

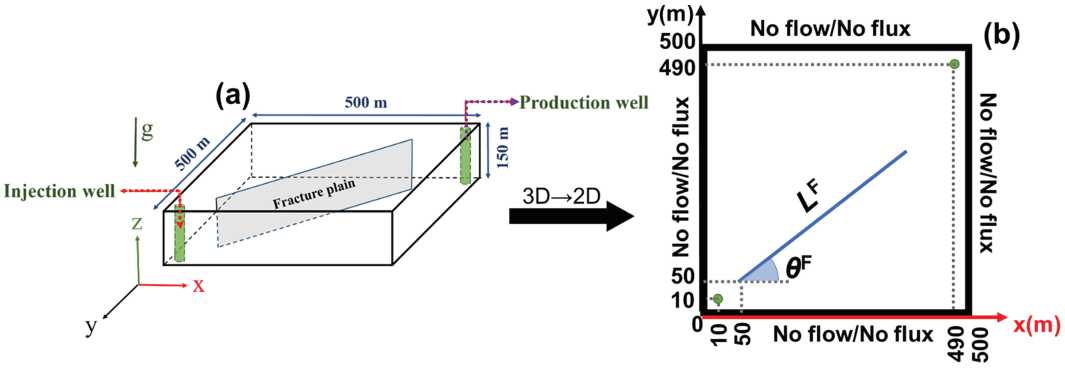


Figure 1: (**a**) 3D schematics of the problem, (**b**) 2D schematics of the reservoir sector with its boundary conditions.

All boundaries are impermeable and thermally insulated. These closed, no-flow/no-flux boundaries are chosen to represent a depleted, structurally bounded reservoir compartment isolated by sealing faults or stratigraphic pinch-outs, which is the target setting motivating this study (small/moderate-scale closed-boundary systems typical of depleted oil/gas reservoirs); this idealization allows the mass and energy balance of the system to be tracked exactly, which is convenient for the UPA/GSA framework, at the cost of neglecting any residual connectivity to the surrounding formation that a real, imperfectly sealed reservoir might have. The matrix is treated as homogeneous but anisotropic, rather than heterogeneous, so that the parametric uncertainty explored here can be attributed unambiguously to the fracture and to a small set of matrix/anisotropy/VGM parameters, isolating the specific research question of fracture-vs-matrix influence from the confounding effect of matrix heterogeneity; introducing matrix heterogeneity is a natural extension of this framework, left for future work. Likewise, the reservoir is initialized brine-saturated at native pressure-temperature conditions, and CO_2 is injected cold and supercritical, in line with the depleted-oil/gas-reservoir GCS scenario adopted from prior closed-reservoir studies [3,38] The reservoir is initially saturated with brine, and an initial pressure of 36.7 MPa and temperature of 420 K (i.e., 147°C) are specified as the initial conditions for every element in the domain. The temperature of the injected CO_2 is specified as 350 K (i.e., 77°C), and CO_2 is kept at a supercritical state by maintaining a pressure above that of critical pressure of 7.38 MPa at the injection well. The injection well is operated under a 36 MPa bottom-hole pressure control which is considstent with the 2 km depth assumption of the reservoirthe production well is operated such that, in this closed, no-flow-boundary domain, the produced brine (and later CO_2) mass balances the injected CO_2 mass over the simulated period. The injected CO_2 gradually displaces brine, and spreads from the injection well to the production well [38], slowly creating a CO_2-dominated media.

2.2 Governing Equations and Numerical Discretization

The problem described in the previous sub-section is numerically simulated using the finite element-based software COMSOL Multiphysics®. The two-phase flow of CO_2 and brine in fractured porous media is governed by the multiphase Darcy's law and mass balance equation [75,76]:

$$\mathbf{u}_\alpha^\beta = \rho_\alpha \frac{k_s k_{r\alpha}^\beta}{\mu_\alpha} \cdot \left(\nabla P_\alpha^\beta - \rho_\alpha^\beta \mathrm{g} \nabla z \right) \tag{1}$$

$$\varphi^\beta \frac{\partial (\rho_\alpha S_\alpha^\beta)}{\partial t} - \nabla \cdot \mathbf{u}_\alpha^\beta = 0 \tag{2}$$

$$S_w^\beta + S_g^\beta = 1 \tag{3}$$

where, P_α^β (Pa) is the pressure of the phase α and medium β. α can have the subscript w for brine as the wetting phase, or the subscript g for CO_2 as the non-wetting phase. The superscript β is associated with fracture (F) and the porous matrix (M) and indicates that Darcy's law was applied to simulate the multiphase flow in both the porous matrix and the fracture. $\mathbf{u}_\alpha^\beta$ (m/s) denotes the Darcy velocity vector of phase α in the media β. μ_α (Pa·s) is the dynamic viscosity of the fluid, and $k_{r\alpha}^\beta$ (-) is the relative permeability. k_s (m/s) is the absolute permeability, g (m/s^2) is the acceleration of gravity, φ^β (-) is the porosity, and ρ_α (kg/m^3) is the density of phase α.

CO_2 and brine densities and viscosities are treated as functions of local pressure and temperature rather than held constant, using COMSOL's built-in real-fluid property libraries for CO_2 and brine; this is important given that pressure and temperature vary over roughly 350–420 K and up to ≈36 MPa in this problem. In this study, the VGM equations [77,78] are used to relate the phase saturations to capillary pressure (P_c^β) (Pa) and relative permeabilities:

$$P_c^\beta = P_d^\beta \left[\left(S_{ew}^\beta \right)^{-1/m^\beta} - 1 \right]^{1/n^\beta} \tag{4}$$

where P_d (Pa) is the non-wetting fluid entry pressure, and n^β (-) and m^β (-) are the VGM parameters, defined as [77]:

$$m^\beta = 1 - \frac{1}{n^\beta} \tag{5}$$

S_{ew}^β (-) in Eq. (4) is the effective water saturation defined as [77]:

$$S_{ew}^\beta = \frac{S_w^\beta - S_{rw}^\beta}{1 - S_{rw}^\beta - S_{rg}^\beta} \tag{6}$$

where S_{rw}^β (-) and S_{rg}^β (-) are the residual saturations of the wetting phase (i.e., brine) and the non-wetting phase (i.e., CO_2), respectively. The relative permeabilities k_{rw}^β (-) and k_{rg}^β (-) are defined in the VGM model as follows: [77]:

$$k_{rw}^\beta = \sqrt{S_{ew}^\beta} \left[1 - \left(1 - {S_{ew}^\beta}^{m^\beta - 1} \right)^{m^\beta} \right]^2 \tag{7}$$

$$k_{rg}^\beta = \sqrt{1 - S_{ew}^\beta} \left(1 - {S_{ew}}^{\beta m^\beta - 1} \right)^{2m^\beta} \tag{8}$$

The heat transfer in the fractured porous media is governed by the following partial differential equation [76]:

$$d_z \left(\rho^\beta C^\beta \right)_{\text{eff}} \frac{\partial T^\beta}{\partial t} + d_z \rho^\beta C^\beta \mathbf{u}^\beta \cdot \nabla \partial T^\beta + \nabla \cdot \mathbf{q}^\beta = f^\beta \tag{9}$$

where T^β (K) is the temperature (i.e., the state variable for heat transfer), d_z (m) is the reservoir thickness, and f^β (W/m^2) is the heat flux source-sink term. ρ^β (kg/m^3) as the bulk density of the media β, C^β (J/kg·K) as the bulk specific heat of the media β, in addition to $\mathbf{u}^\beta$ (m/s) (i.e., the total phase transport flux) and $\mathbf{q}^\beta$ (W/m) (i.e., the dispersive heat flux), are given as following [76]:

$$\rho^\beta = \varphi^\beta S_w^\beta \rho_w + \varphi^\beta S_g^\beta \rho_g + \left(1 - \varphi^\beta \right) \rho_s \tag{10}$$

$$C^\beta = \varphi^\beta S_w^\beta C_w + \varphi^\beta S_g^\beta C_g + \left(1 - \varphi^\beta \right) C_s \tag{11}$$

$$\mathbf{u}^\beta = \varphi^\beta S_w^\beta \mathbf{u}_w^\beta + \varphi^\beta S_g^\beta \mathbf{u}_g^\beta \tag{12}$$

$$\mathbf{q}^\beta = -d_z \boldsymbol{D}^\beta \nabla \partial T^\beta \tag{13}$$

where ρ_w (kg/m^3), ρ_g (kg/m^3) and ρ_s (kg/m^3) are the brine, CO_2, and grain densities, respectively. Moreover, C_w (J/kg·K), C_g (JI/kg·K) and C_s (J/kg·K) are the specific heat of brine, CO_2, and the porous grains, respectively. $\boldsymbol{D}^{\beta}$ (W/mK) is the bulk thermal conductivity, defined as:

$$\boldsymbol{D}^{\beta} = \varphi^{\beta} S_w^{\beta} D_w \boldsymbol{I} + \varphi^{\beta} S_g^{\beta} D_g \boldsymbol{I} + \left(1 - \theta_{\mathrm{p}}\right) D_S \boldsymbol{I} + \boldsymbol{D}_{\mathrm{disp}}^{\beta} \tag{14}$$

$$D_{\mathrm{disp}}^{\beta} = \left(\alpha_L^{\beta} - \alpha_T^{\beta}\right) \frac{\mathbf{u}^{\beta} \times \mathbf{u}^{\beta}}{|\mathbf{u}^{\beta}|} + \alpha_T^{\beta} |\mathbf{u}^{\beta}| \tag{15}$$

where D_w (W/mK), D_g (W/mK) and D_s (W/mK) are the conductivity of brine, CO_2, and grains, respectively. $D_{\mathrm{disp}}^{\beta}$ (W/m·K) is the dispersive heat conductivity of the fluid and α_L^{β} (m) and α_T^{β} (m) are the longitudinal and transverse dispersivity coefficients of the β medium, respectively.

COMSOL, as mentioned earlier, has been used for the spatial and temporal discretization and the simulation process. In recent years, geoscientists have increasingly shown interest in COMSOL. One of the primary benefits of COMSOL is its versatility, as it offers a variety of physical modules and the ability to couple them with different physics and geometries. The abilities of COMSOL has been evaluated and highlighted by the authors of this work previously on coupled transport processes in porous media and fractured porous media [79–81]. The COMSOL model of our case study is created by coupling the 'Phase Transport in Porous Media' and the 'Heat Transfer in Porous Media' modules. The 'Multiphase Flow in Porous Media' interface combines 'Darcy's Law interface' with the 'Phase Transport in Porous Media interface' to model the flow and transport of multiple immiscible phases in a fractured porous medium. Consistent with this immiscible two-phase formulation, CO_2 dissolution into brine, solubility (dissolution) trapping, residual (capillary) trapping beyond that captured by the VGM relative permeability curves, mineral trapping and associated geochemical reactions, and leakage through the caprock or bounding faults are not represented in the present model, although these mechanisms can be important where fault zones bound the reservoir and are themselves a source of uncertainty. This is a reasonable simplification for a first, sensitivity-oriented study focused on the free-phase CO_2 and heat transport controlled by the explicit fracture, but it implies that the reported stored-CO_2-mass metrics correspond to free-phase (structural/hydrodynamic) trapping only, and the absolute stored-mass values would be expected to increase, and the associated uncertainty to change, once dissolution and mineral trapping are accounted for in future extensions of this work [82]. The 'Heat Transfer in Porous Media' interface is used to model heat transfer by both conduction and convection mechanisms. The temperature equation in porous media corresponds to the advection-conduction/dispersion equation with thermodynamic averaging model properties to account for both solid matrix and fluid properties. The simulations are done using the 'Time Domain' module of COMSOL for delivering the temporal response of phase transport and heat transfer. Numerical simulations are carried out with a triangular irregular mesh generated by the COMSOL meshing tool. The domain is discretized into approximately 20,000 to 23,000 elements (i.e., depending on the fracture geometry the number of elements vary) (Fig. 2a), of which approximately half belong to the discretization of the fracture (Fig. 2b). The mesh is highly refined inside and in the vicinity of the fracture. The reason for this mesh grid distribution is that the phase transport and heat transfer produce a highly variable gradient near the fracture. The simulation period is considered 10,000 days (approximately 27 years). The time steps are adapted by COMSOL for better convergence and faster simulation (i.e., less computation effort). The values of fixed model input parameters are presented in Table 1. A brief mesh sensitivity analysis is given in the Appendix A which shows that the results are not sensitive to the grid size and element number in the range that we have considered for our simulations. Fig. A1 shows that the point-wise saturation and temperature time series, and the mass/heat-loss/heat-flux metrics, are stable and effectively independent of grid size over the tested range. Fig. A2 confirms this at the spatial level,

showing that the 50% CO_2 saturation and 400 K temperature contour lines are essentially unchanged across mesh refinements from approximately 4000 to 40,000 elements.

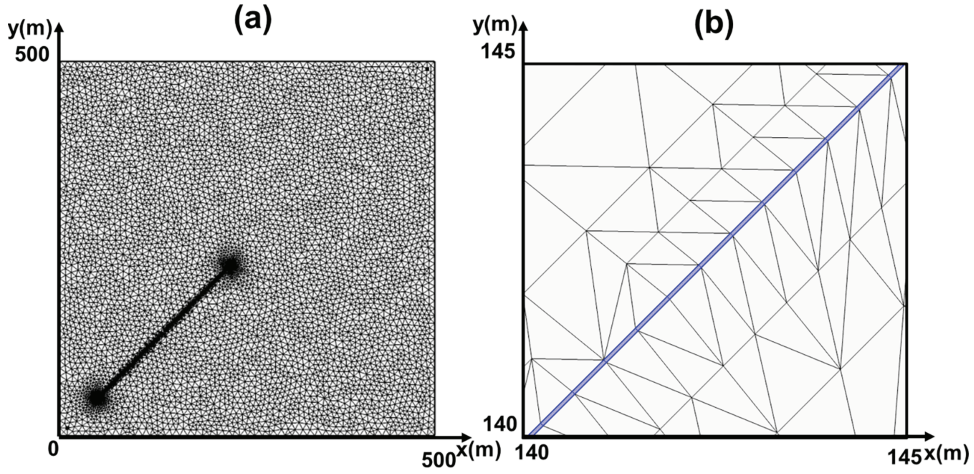


Figure 2: Numerical discretization of the problem: (**a**) The whole domain and (**b**) a zoomed square near the fracture.

Table 1: Fixed input parameter values in the simulation of the reservoir.

Parameter	Value	Unit
Formation		
Reservoir dimensions*	500 × 500 × 150	m
Reservoir thickness**	150	m
Rock grain density*	2650	kg/m^3
Rock specific heat*	1000	J/kg/K
Rock thermal conductivity*	2.1	W/m/K
Porous matrix porosity**	0.2	–
Initial conditions*		
Average reservoir pressure (P_{in})**	36.7	MPa
Reservoir temperature***	420.15	K
Production/injection		
Injector–producer distance*	707.1	m
Injection temperature (T_{inj})*	350	K
Fracture***		
Fracture porosity***	1.0	–
Well radius*	0.1	m

Note: *[83]; **[84]; ***[85].

The fixed parameter values in Table 1 are not all drawn from a single field: the reservoir/rock properties and initial conditions follow and, two widely used reference case studies for CO_2-based geothermal systems in generic sedimentary reservoirs, while the fracture porosity follows the discrete-fracture modeling study of. These sources were chosen because they provide an internally consistent, previously validated parameter set for the type of CO_2-brine-heat problem addressed here, rather than because they describe one specific field site; the resulting reservoir is therefore best regarded as a realistic but generic depleted reservoir

analogue, consistent with the preliminary, sensitivity-oriented scope of this study rather than a site-specific assessment [83–85].

2.3 Uncertain Input Parameters and Output Metrics

Eight input parameters are assumed to be uncertain. These parameters can be classified into three groups: (1) selected fracture properties, including fracture angle (θ^F), length (L^F), and aperture (ω^F), (2) porous matrix properties, including permeability (k^M), anisotropy ($r_K = k_y^M/k_x^M$), and the VGM parameter n^M (see Eqs. (3) and (4)) the thermal transfer-based parameters including: longitudinal (α_L) and transverse (α_T) dispersivities. The uncertainty of these parameters is characterized by either uniform or log-uniform distributions, as described in Table 2.

Table 2: Characteristics of the hypothetical PDFs of the uncertain input parameters.

Parameter	PDF Type	Min	Max	Value in Deterministic Simulation	Unit
Longitudinal dispersivity (α_L^M)	Log-uniform	0.1	1	0.55	m
Transverse dispersivity (α_T^M)	Log-uniform	0.1	1	0.55	m
Reservoir permeability (k^M)	Log-uniform	10^{-14}	10^{-11}	$10^{-12.5}$	m^2
Reservoir anisotropy (r_K)*	Log-uniform	0.1	10	5.05	–
Fracture aperture (w^F)	Log-uniform	10^{-4}	3.16×10^{-3}	1.63×10^{-3}	m
Fracture length (L^F)	Uniform	100	400	250	m
VGM parameter (n^M)	Uniform	2	5	3.5	–
Fracture rotation angle (θ^F)	Uniform	10	80	45	degree

Note: *This is the ratio between k^M in the x and y directions = k_y^M/k_x^M.

The model output QoIs (a.k.a. metrics) for this problem are chosen as follows:

- The *non-dimensional mass of stored* CO_2 in the reservoir after 2000 and 10,000 days, which are denoted by $\overline{M}_{CO_2}^{2000d}$ (-) and $\overline{M}_{CO_2}^{10000d}$ (-), respectively. This QoI is normalized by dividing by the mass of the reservoir pores filled with CO_2 (i.e., assuming CO_2 fills the reservoir pore volume). $\overline{M}_{CO_2}^{2000d}$ is chosen to represent the early stages of CO_2 sequestration, and $\overline{M}_{CO_2}^{10000d}$ pertains to the final state of CO_2 storage in the reservoir.
- The *non-dimensional heat loss* of the reservoir after 2000 and 10,000 days, denoted by $\overline{V}_T^{2000d}$ (-) and $\overline{V}_T^{10000d}$ (-), respectively. The non-dimensional heat loss is calculated by dividing the volume of the reservoir with temperature reduced to below 127°C, by the total reservoir volume, and represents the fraction of the reservoir cooled down during a given period.
- Brine-based *heat flux in the production well* (Wm^{-2}) after 2000 and 10,000 days, denoted by ${Q_T}^{2000d}$ (Wm^{-2}) and ${Q_T}^{10000d}$ (Wm^{-2}), respectively. These QoIs represent the amount of heat that can be produced from hot brine during a given period of CO_2 sequestration.
- Time (d) (after the start of CO_2 injection) for which the CO_2 cut in the produced fluid reaches 0.8. This is denoted by $T_{80\%}$ (d) and marks approximately the end of the sequestration phase.

For the minority of realizations in which the 0.8 CO_2-cut threshold is not reached within the 10,000-day simulated window, T80% is obtained by extrapolating the simulated CO_2-cut-vs-time curve using a fitted logistic/exponential trend beyond t = 10,000 days. This metric therefore carries added uncertainty for the

slowest-breakthrough realizations, consistent with it showing the highest coefficient of variation among all output metrics (Table 3); this caveat is noted when interpreting the T80% results.

Table 3: Statistical characteristics of the metrics.

	Range	Minimum	Maximum	Mean	Standard Deviation	Coefficient of Variation	Skewness
$\overline{M}_{CO_2}^{2000d}$ (-)	0.0024	0.1664	0.1688	0.1687	0.00052	0.0031	−0.4220
$\overline{M}_{CO_2}^{10000d}$ (-)	0.0717	0.3664	0.4381	0.4277	0.011234	0.0262	−2.2571
$\overline{V}_T^{2000d}$ (-)	0.0272	0.0260	0.0532	0.0345	0.0045323	0.1312	0.8955
$\overline{V}_T^{10000d}$ (-)	0.2596	0.1180	0.3776	0.1802	0.0431018	0.2391	1.1000
$Q_T{}^{2000d}$ (Wm^{-2})	176.9866	84.4670	261.4537	182.3486	32.8690	0.1802	−0.2691
$Q_T{}^{10000d}$ (Wm^{-2})	120.6208	42.8311	163.4519	101.7982	20.4874	0.2012	0.0772
$T_{80\%}$ (d)	13,298	172	13,470	4972	2528	0.5054	0.3943

3 Global Sensitivity Analysis Based on Polynomial Chaos Expansion

In this study, the variance-based Sobol indices are employed to assess the sensitivity of the output QoIs described in Section 2.3 to the uncertain model inputs explained in Section 2.2. Assuming that $y = f(x)$ is a square-integrable function with mutually independent inputs $x = \{x_1, \ldots, x_n\}$, the variation of y (represented by $V(y)$) can be broken down into [86]:

$$V(y) = \sum_{i=1}^{n} V_i + \sum_{i_1=1}^{n} \sum_{i_2=i_1+1}^{n} V_{i_1 i_2} + \sum_{i_1=1}^{n} \sum_{i_2=i_1+1}^{n} \sum_{i_3=i_2+1}^{n} V_{i_1 i_2 i_3} + V_{i_1 \ldots i_n} \tag{16}$$

where V_i is the variance of y with respect to each single input x_i, and $V_{i_1 \ldots i_k}$ denotes the y's variance with respect to the interaction of $\{x_1, \ldots, x_k\}$. Eq. (16) can be normalized by dividing by $V(y)$. The resulting first-order main-effect Sobol sensitivity index of an input x is defined as [63]:

$$S_i = \frac{V_{x_i}\left(E_{x_{-i}}\left(yx_i\right)\right)}{V(y)} \tag{17}$$

And the total Sobol sensitivity of index of an input x is defined as [63]:

$$S_i^T = 1 - \frac{V_{x_{-i}}\left(E_{x_i}\left(yx_{-i}\right)\right)}{V(y)} \tag{18}$$

where x_{-i} denotes all model inputs except for x_i, S_i^1 is the sole contribution of x_i to the variance of y neglecting its interactions with other inputs, and $E()$ denotes the expected value. Higher order sensitivity indices to input interactions are represented by the remainder of terms in Eq. (16) divided by $V(y)$. The total-order or total-effect Sobol sensitivity index describes the overall contribution of a parameter x_i to the output variance, which includes both its individual effect and its interactions with the other input parameters. It is defined by [87].

In this study, the SALib python package [88] is employed for the calculation of the Sobol indices.

Estimation of the first-order and total Sobol sensitivity indices in Eqs. (17) and (18) are often carried out via the Monte Carlo method [89], which requires repeated evaluations of the numerical model. The resulting high, sometimes intractable computational computation time can be reduced through data-driven surrogate models [90] such as the non-intrusive PCEs. The PCE surrogate model expresses the stochastic simulation output y as [91]:

$$y = \sum_{i=0}^{\infty} \alpha_i \psi_i(\zeta) \tag{19}$$

The elements of the above series include the deterministic coefficient and the stochastic orthogonal polynomial, where is a random variable with a predefined probability distribution. The choice of the type of orthogonal polynomial used in constructing PCEs is dictated by the probability distribution of [92]. Based on the assumption that the probability distributions describing the unknown inputs are uniform, the 'Legendre polynomials' are used in this study. Five of the eight uncertain parameters (αL, αT, kM, rK and ωF, see Table 2) are characterized by log-uniform distributions; for these parameters, the input is first transformed to, and sampled in, log-space, in which the distribution is uniform, before the Legendre-based PCE is constructed. The remaining parameters (LF, nM and θF) are directly uniform and require no transformation.

Non-intrusive PCEs consider the physics of the system as a black box and use known input-output pairs as a training dataset for the estimation of α_i e.g., the regression approach. The steps in this procedure are as follows: (1) deterministic or random sampling methods are used to select a set of n_r regression points (each indicated by ε_k) from the probability space of the random input variable(s). (2) The same numerical simulations are carried out using these regression points. The model outputs are presented for these $n_r$simulations as $y(\varepsilon_k)$. (3) The following least square optimization problem is solved to estimate the PCE coefficients α_i [90]:

$$\min \sum_{k=1}^{n_r} \left[y(\varepsilon_k) - \sum_{k=0}^{g} \alpha_i \psi_i(\varepsilon_k) \right]^2 \tag{20}$$

The python package 'ChaosPy' [93] is employed to construct the PCE surrogate models in this study.

The PCE surrogate for each output metric is built as a 4th-order full PCE (where all possible terms are taken into account), following the approach of Koohbor et al. (2019). These models are constructed using regression (collocation) points drawn from the same 1000-realization Monte Carlo ensemble used for the UPA. The fit quality and predictive accuracy of each surrogate are assessed through the PCE-vs-COMSOL diagrams shown in Appendix B in Fig. A3. Excellent fit results (R^2 values greater than 0.9) were obtained for all seven output metrics, supporting the reliability of the Sobol sensitivity rankings derived from the surrogate models.

4 Results and Discussion

4.1 Deterministic Simulation

As an example and for minor representation of the spatial simulation by using mean values of the uncertain input parameters (i.e., geometric mean for the reservoir permeability, and arithmetic mean for the rest, as presented in Table 2), CO_2 sequestration in the reservoir is simulated for 10,000 days. Fig. 3 shows the CO_2 phase saturation distribution at 1000, 2000, 3000, 5000, 7000, and 10,000 days, respectively, after the onset of CO_2 injection. As demonstrated, the CO_2 plume expands over time and occupies an increasingly larger portion of the reservoir volume. The CO_2 plume tends to move in the direction of the fracture faster and further than the surrounding porous matrix due to the significantly higher permeability of the fracture;

therefore, the plume is elongated towards the production well in the direction of the fracture as can be seen. When the CO_2 plume front passes the fracture region, it is dispersed proportionally to its advancement path. This can be attributed to the significantly lowered fluid velocity, decreased phase gradient, and higher VGM parameter (n^M) value in the porous matrix compared to the fracture.

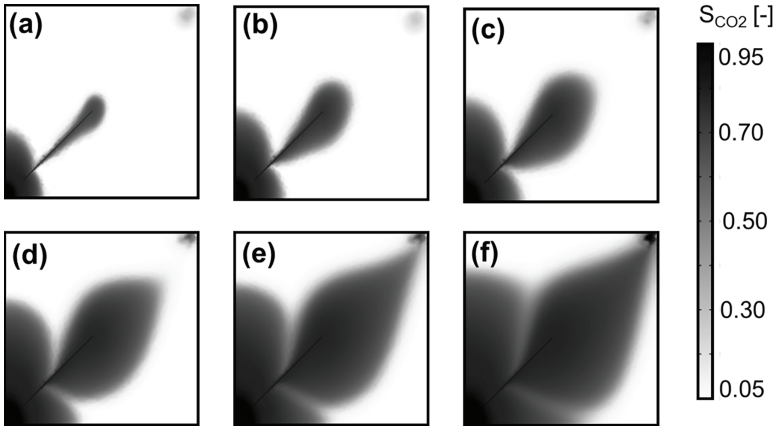


Figure 3: CO_2 phase saturation distribution at: (**a**) 1000, (**b**) 2000, (**c**) 3000, (**d**) 5000, (**e**) 7000, and (**f**) 10,000 days.

Fig. 4 shows the temperature distribution at 1000, 2000, 3000, 5000, 7000, and 10,000 days, respectively, after the onset of CO_2 injection. The thermal loss plume along with the distribution of temperature variation can be seen in Fig. 4 during the simulation period. The thermal loss (i.e., the heat lost due to the replacement of hot brine with cold CO_2) has the highest gradient along the fracture orientation. A dispersivity depends on the Darcy velocity and is hence directly proportional to permeability [94,95], high permeability and high dispersivity in the fracture complement each other in causing a high heat dispersion, and it is observed that the cold plume is elongated along the fracture. The elliptical shape of the cold plume inside the porous matrix is related to the effect of anisotropy and its impact on the thermal dispersion in the and directions.

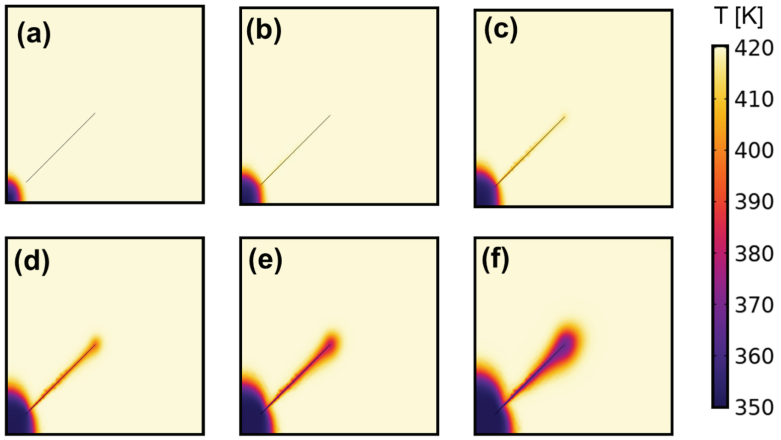


Figure 4: Temperature distribution at: (**a**) 1000, (**b**) 2000, (**c**) 3000, (**d**) 5000, (**e**) 7000, and (**f**) 10,000 days.

Figs. 5 and 6 show temporal variations of CO_2 saturation and temperature at three observation points, namely: (a) the starting point of the fracture that is closest to the injection well (), which is denoted by, (2) at the other end point of the fracture () denoted by, and (c) the production well location () denoted by. In Fig. 5a, a breaking point in the CO_2 saturation curve at point is observed at approximately days, indicating that at

this point, the CO_2 plume front has passed. As the breaking point in is seen at approximately 5000 days (see Fig. 5b), it can be inferred that the CO_2 plume transition in the fracture happens mainly between the breaking points of the two ends of the fracture corresponding to 3000 and 5000 days, and the full length of the fracture serves as a conduit for CO_2 transport after t = 5000 days. The rate of change in CO_2 saturation at is lower than that of, which is related to the high flow velocity in the fracture compared to the porous matrix. The temporal change of CO_2 saturation at the production well (Fig. 5c) resembles that of, because the long time it takes for CO_2 to travel between the fracture and the production well diminishes the local effect of the fracture, and flow in the porous matrix becomes dominant. Comparing Fig. 6a,b shows that temperature tends to decrease faster in than, because due to higher heat dispersion in the fracture compared to the porous matrix, the temperature variation in the cold front becomes more dispersed in the fracture. At the production well, the temperature breakthrough curve (Fig. 6c) shows a delayed and more gradual decline than at either fracture endpoint, reflecting the combined travel time and dispersion accumulated along the full flow path from the injection well.

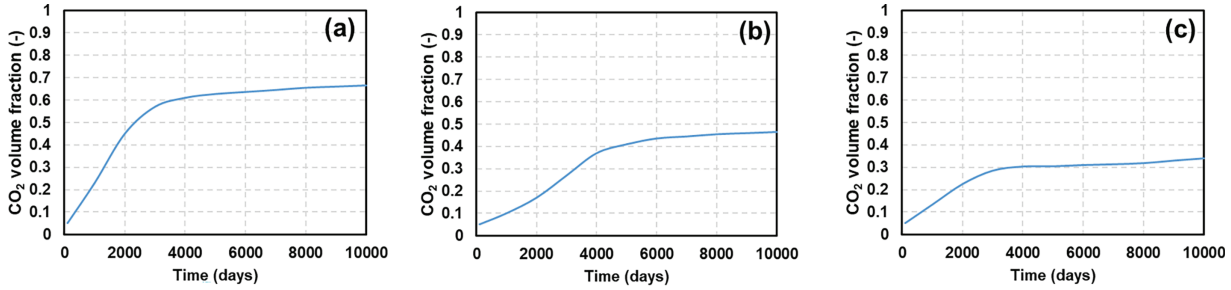


Figure 5: CO_2 saturation vs. time at (**a**) the end of the fracture that is closest to the injection well, (**b**) the other end of the fracture, and (**c**) the production well.

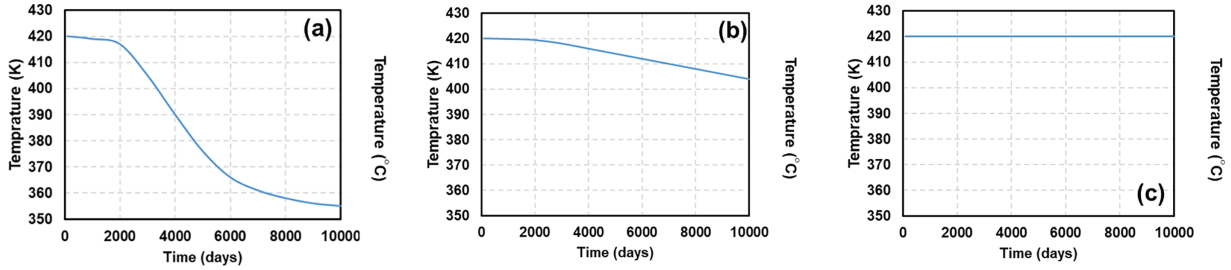


Figure 6: Temperature breakthrough curve at (**a**) the end of the fracture that is closest to the injection well, (**b**) the other end of the fracture, and (**c**) the production well.

4.2 Uncertainty Quantification

The results of Monte Carlo-based UPA are presented as probability density functions (PDFs) of the output QoI in Fig. 7. Key statistical attributes of these PDFs are given in Table 3. Based on Table 3, the QoIs with the least uncertainty are related to the mass of stored CO_2, namely (Fig. 7a,b), both of which have a right-skewed PDF. Fig. 7c has a moderate CV, with a PDF skewed to the left. Fig. 7d has the second highest uncertainty among all metrics, with a PDF notably skewed to the left. Fig. 7e has a CV comparable to that of Fig. 7c, with a nearly symmetric PDF that is slightly skewed to the right. Fig. 7f comes in third place in terms of uncertainty, and has a rather symmetric PDF. The metric (Fig. 7g) has the highest value of the coefficient of variation (CV), and hence the highest uncertainty; its PDF is slightly skewed to the left.

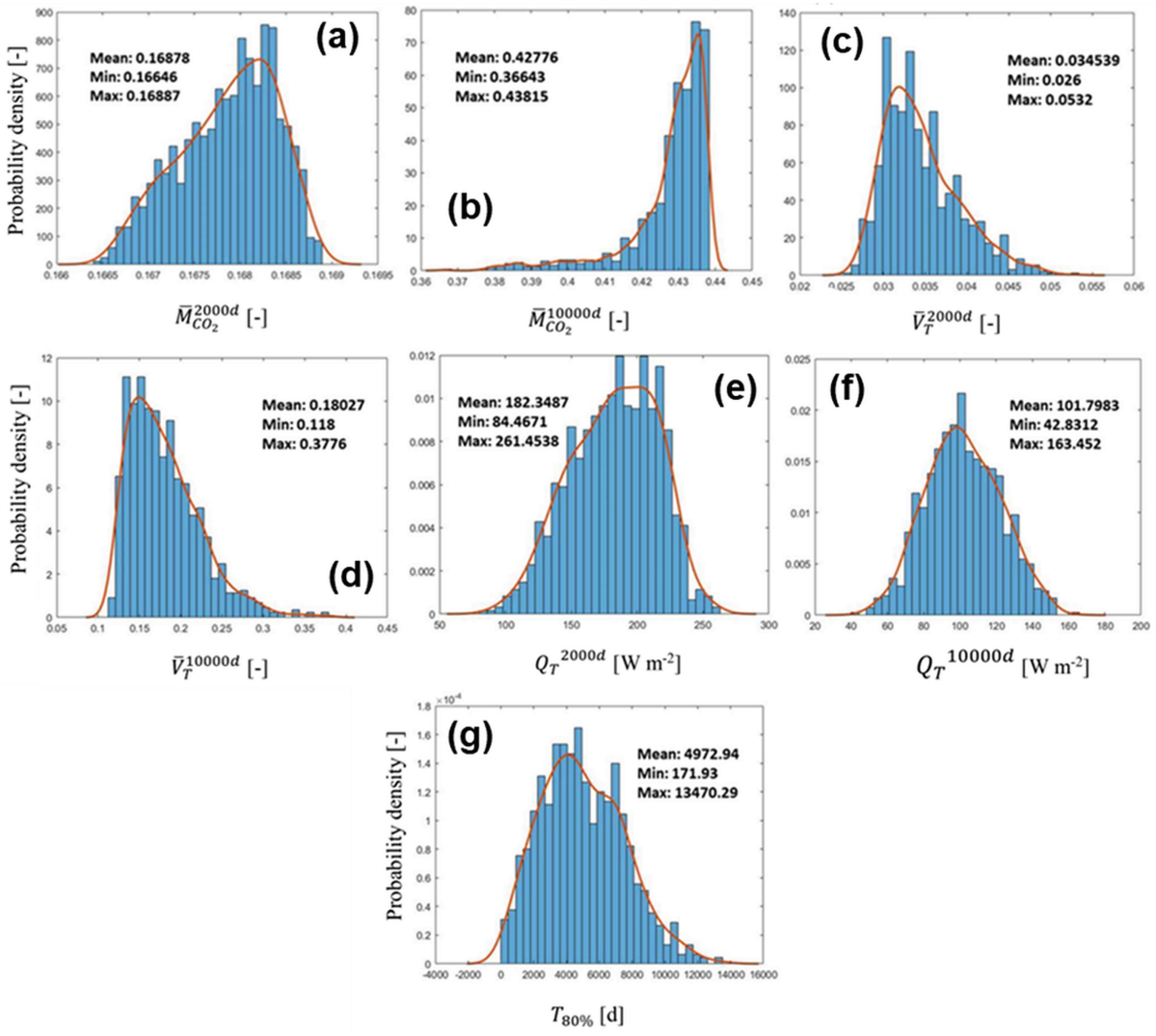


Figure 7: The probability distribution of (**a**) $\overline{M}_{CO_2}^{2000d}$ (**b**) $\overline{M}_{CO_2}^{10000d}$ (**c**) $\overline{V}_T^{2000d}$ (**d**) $\overline{V}_T^{10000d}$ (**e**) $Q_T{}^{2000d}$ (**f**) $Q_T{}^{10000d}$ (**g**) $T_{80\%}$, obtained from MCS-based UPA.

4.3 Sensitivity Analysis Results

In this subsection, the GSA results are presented and analyzed to better understand how the model's output values can be assigned to model inputs. Fig. 7 shows the distribution of the metrics in respect to the values calculated and Fig. 8 shows the stacked bars of first-order and total Sobol indices for all the metrics in respect to the input parameters. The values are given in Tables 4 and 5. As shown, stacked bars of the first-order and total-order show indices are similar for most parameters and metrics. Values of the total indices are higher than those of the first-order indices, indicating some interaction effects between the uncertain input parameters. These trends are visualized in Fig. 8, which compares the first-order and total Sobol indices of all eight uncertain parameters across the seven output metrics.

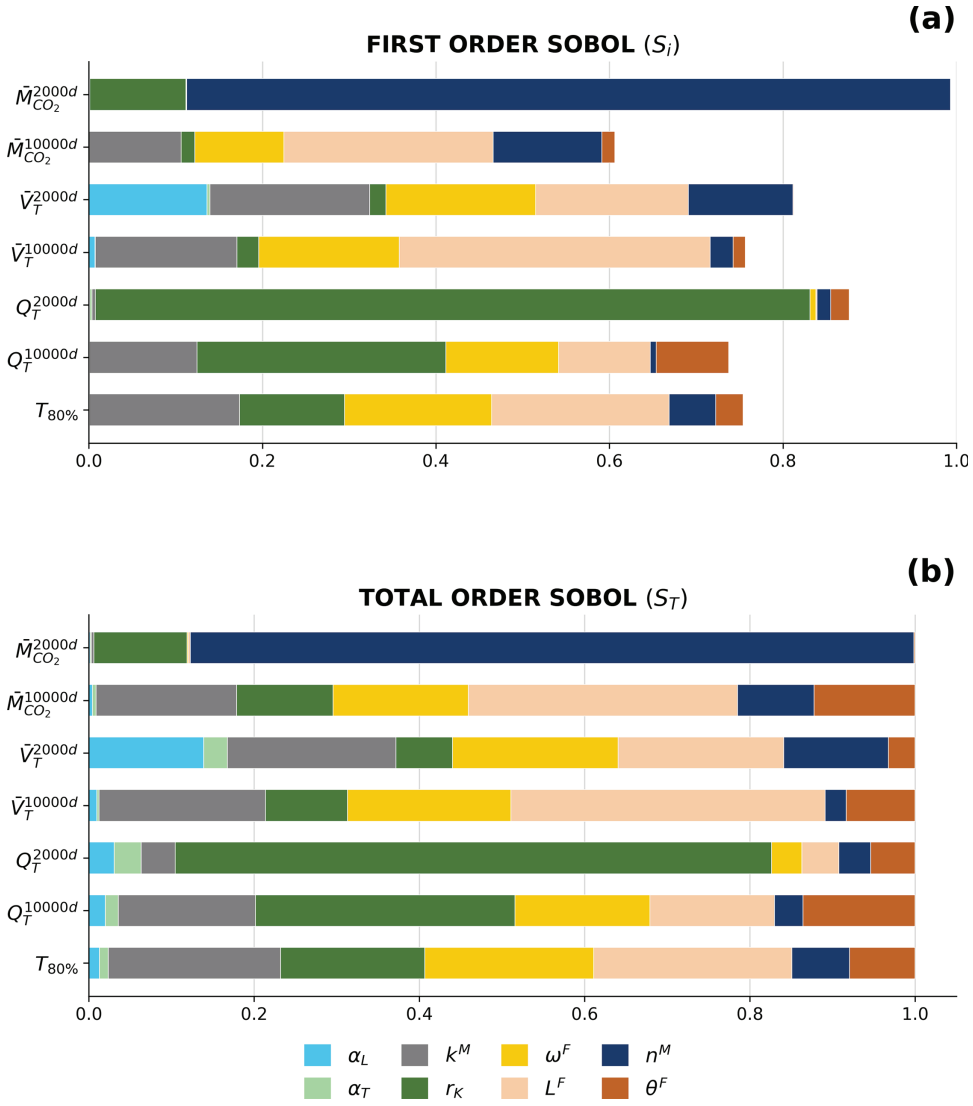


Figure 8: Sobol indices for different parameters: (**a**) First order Sobol' index and (**b**) total Sobol' index.

Table 4: First-order Sobol indices for the output QoIs.

Column1	α_L^M	α_T^M	k^M	r_K	w^F	L^F	n^M	θ^F
$\overline{M}_{CO_2}^{2000d}$ (-)	0.00022	0.00003	8.40×10^{-4}	0.110731	0.00042	0.00051	0.88034	0.0002
$\overline{M}_{CO_2}^{10000d}$ (-)	0.00005	0.00042	1.06×10^{-1}	0.015842	0.10263	0.24120	0.12515	0.0149
$\overline{V}_T^{2000d}$ (-)	0.13615	0.00350	1.84×10^{-1}	0.018856	0.17252	0.17592	0.12052	0.0009
$\overline{V}_T^{10000d}$ (-)	0.00736	0.00042	1.63×10^{-1}	0.025079	0.16198	0.35824	0.02648	0.0140
$Q_T{}^{2000d}$ (Wm^{-2})	0.00126	0.00264	3.83×10^{-3}	0.82369	0.00646	0.00149	0.01568	0.0213
$Q_T{}^{10000d}$ (Wm^{-2})	0.00005	0.00069	1.24×10^{-1}	0.286867	0.12972	0.10581	0.00697	0.0833
$T_{80\%}$, (d)	0.00031	0.00044	1.73×10^{-1}	0.120888	0.16984	0.20451	0.05365	0.0314

Table 5: Total order Sobol indices for the output QoIs.

	α_L^M	α_T^M	k^M	r_K	w^F	L^F	n^M	θ^F
$\overline{M}_{CO_2}^{2000d}$ (-)	1.59×10^{-3}	0.00169	0.00293	0.113604	0.00171	0.00270	0.88281	0.0016
$\overline{M}_{CO_2}^{10000d}$ (-)	6.86×10^{-3}	0.00623	0.25345	0.174228	0.24472	0.48524	0.13843	0.1824
$\overline{V}_T^{2000d}$ (-)	0.1709594	0.03484	0.25068	0.083861	0.24633	0.24576	0.15578	0.0397
$\overline{V}_T^{10000d}$ (-)	0.0123626	0.00361	0.25766	0.126455	0.25315	0.48609	0.03241	0.1069
${Q_T}^{2000d}$ (Wm^{-2})	3.67×10^{-2}	0.03830	0.04894	0.855514	0.04360	5.29×10^{-2}	0.04575	0.0637
${Q_T}^{10000d}$ (Wm^{-2})	2.63×10^{-2}	0.02106	0.21933	0.414516	0.21622	0.19877	0.04581	0.1792
$T_{80\%}$ (d)	0.0168475	0.01394	0.269785	0.225565	0.26456	0.31034	0.09052	0.1028

The most influential parameter on $\overline{M}_{CO_2}^{2000d}$ is n^M followed by fracture length, reservoir permeability, and fracture aperture. The CO_2 plume travels faster along the fracture, and the advancement depends directly on the length of the fracture. A longer fracture means the plume travels mainly along the fracture and occupies less volume in the porous matrix until it reaches the production well and exits.

The most influential parameters on heat loss after 2000 and 10,000 days are k^M and L^F, respectively. This shows that the flow of the cold CO_2 is dominated by matrix porosity before and around the time the CO_2 front reaches the fracture, and by fracture porosity later on. ${Q_T}^{2000d}$ is most sensitive to reservoir anisotropy. Flow near the production well is significantly affected by anisotropy of the porous matrix before the effect of the fracture is observed. As time passes, flow direction and cold plume migration become more affected by the fracture properties (most notably, fracture length and aperture). Hence, though ${Q_T}^{10,000d}$ is still dominated by the affected of anisotropy, its sensitivity to geometric fracture parameters is significant. The sensitivity of $T_{80\%}$ is not dominated by a single input parameter, and L^F, k^M, t^F, and r_K have a significant influence on $T_{80\%}$.

5 Conclusion

Depleted oil and gas reservoirs are viable targets for coupled CO_2 sequestration, and many also hold potential for geothermal energy extraction from the co-produced hot brine. This work presents a theoretical analysis of CO_2 sequestration in an explicitly defined, single-fractured reservoir with closed boundaries. The goal was to systematically assess how uncertainty in fracture and matrix parameters affects the key metrics of this coupled phase-transport and heat-transfer problem, namely CO_2 sequestration and brine-based geothermal energy extraction. The governing equations were first formulated and discretized in a two-dimensional, explicitly fractured domain using the finite-element software COMSOL Multiphysics®. One thousand simulations were then performed across eight uncertain input parameters, from which seven output metrics were computed. Polynomial chaos expansion (PCE) was used to build a surrogate meta-model for each metric, enabling efficient post-processing sensitivity analysis. Sobol' indices (first-order and total-order) were then calculated for each metric with respect to the eight uncertain parameters, and the results were used to assess the relative importance of each parameter.

The simulation results show that the presence of a fracture significantly affects both the phase and temperature distributions within the reservoir. The CO_2 plume propagates markedly faster along the fracture than through the surrounding porous matrix and becomes elongated toward the production well, with the fracture acting as a preferential flow conduit. This conduit behavior accelerates both CO_2 sequestration and

geothermal production. It is, however, a double-edged effect: rapid CO_2 migration is undesirable from a containment standpoint, whereas it is advantageous when the objective is efficient extraction of the hot brine's thermal energy. In either case, the presence of a fracture shortens the operational timescale and can substantially affect reservoir efficiency and productivity, depending on the application. The results further show that predictive uncertainty in key metrics, namely the mass of stored CO_2, reservoir heat loss, production-well heat flux, and the duration of the sequestration phase, is strongly influenced (and in some cases dominated) by uncertainty in fracture properties, underscoring the importance of accurate fracture characterization when modeling coupled sequestration and geothermal energy production. This finding, however, is derived from a single, straight fracture of prescribed length, aperture, and orientation, and should therefore not be over-generalized: in a setting with a connected fracture network rather than a single conduit, the relative influence of fracture vs. matrix parameters on these metrics would likely differ, and quantifying that difference remains an important direction for future work.

The present study should be regarded as a preliminary investigation of coupled phase-transport and heat-transfer simulation for hot-brine extraction during CO_2 sequestration in depleted oil and gas reservoirs. It nonetheless demonstrates the value of PCE-based GSA for characterizing multiple sources of uncertainty in highly nonlinear, coupled physical processes, and the proposed methodology can be readily extended to more complex problems that more closely reflect real-world reservoir engineering and geothermal energy production settings. Regarding the deterministic solver used here, COMSOL proved effective for this preliminary coupled study; for larger or more complex problems, however, more advanced numerical tools and discretization techniques would likely be required for efficient and accurate modelling. Beyond the polynomial-chaos-based approach adopted here, deep-learning and other data-driven surrogate models are increasingly used to accelerate uncertainty quantification and data assimilation in coupled subsurface flow and geomechanics problems [96–99], and coupling such surrogates with the present fracture-explicit framework is a promising direction for extending this work toward field-scale, network-fractured reservoirs.

Acknowledgement: The authors gratefully acknowledge Mohammad Mahdi Rajabi for his insightful comments and valuable advice, particularly regarding the development of the surrogate model.

Funding Statement: The authors received no specific funding for this study.

Author Contributions: The authors confirm contribution to the paper as follows: Ali Bozorgpour: methodology, software, investigation, Writing. Behshad Koohbor: conceptualization, methodology, supervision, Writing. All authors reviewed and approved the final version of the manuscript.

Availability of Data and Materials: The datasets generated and/or analyzed during the current study, together with the numerical model files and associated post-processing materials (including Monte Carlo simulation outputs and PCE/Sobol analysis scripts), are available from the authors upon reasonable request, subject to verification and any applicable data-sharing requirements.

Ethics Approval: Not applicable. This study did not involve human participants, human data, or animals.

Conflicts of Interest: The authors declare no conflicts of interest.

Appendix A

A mesh sensitivity analysis of the results was performed over one order of magnitude of element numbering (i.e., from approximately 4000 to 40,000 elements); the element numbering used for the simulations (i.e., 20,000 to 23,000) lies in the middle of this range, and the results are presented below:

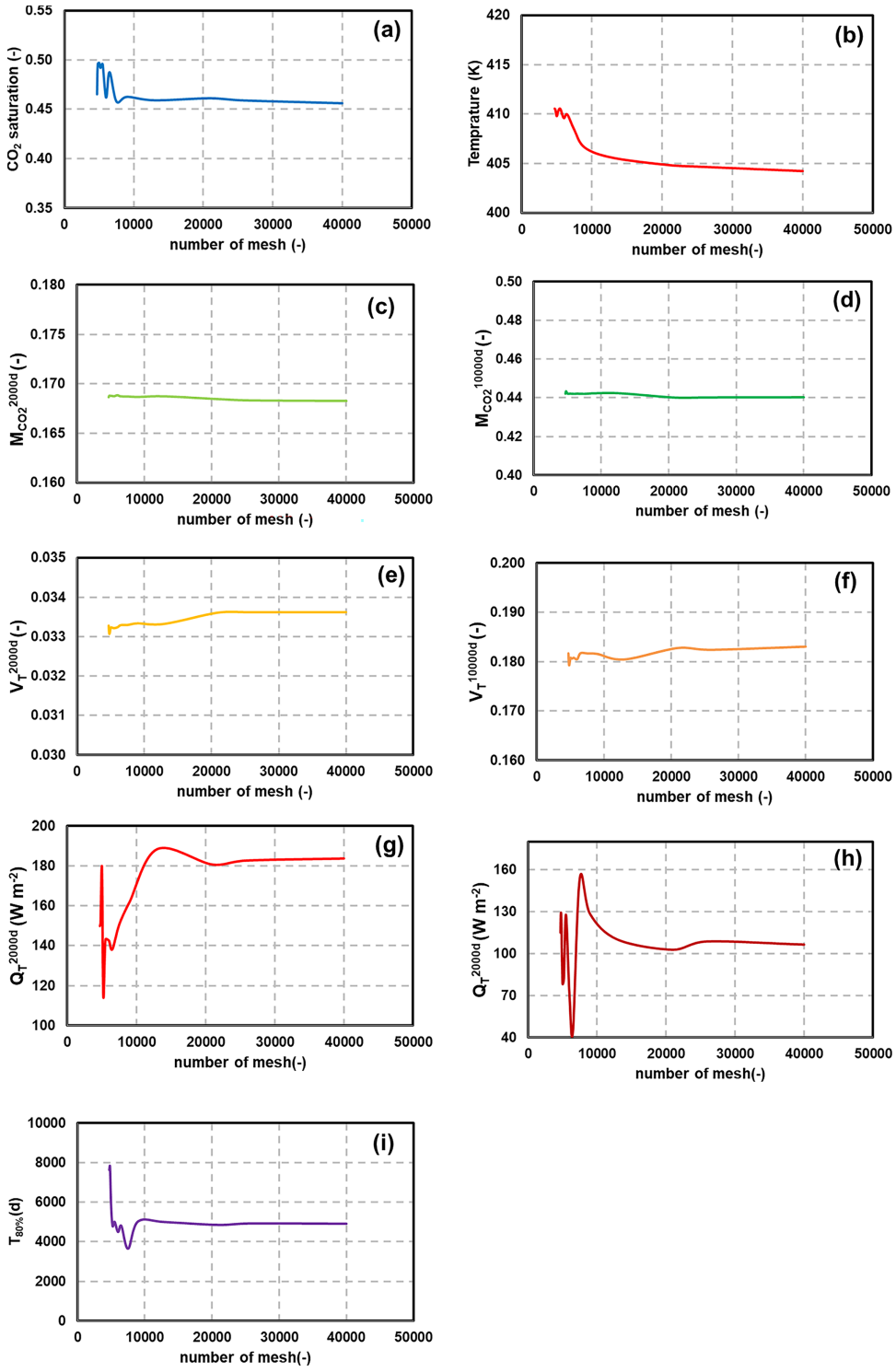


Figure A1: The sensitivity of certain outputs to the number of elements in the simulations: (**a**) The saturation of carbon dioxide in the mid-point of domain (250 m, 250 m), (**b**) temperature of the mid-point in the domain (250 m, 250 m), (**c**) $\overline{M}_{CO_2}^{2000d}$ (-), (**d**) $\overline{M}_{CO_2}^{10000d}$, (**e**) $\overline{V}_T^{2000d}$ (-), (**f**) $\overline{V}_T^{10000d}$, (**g**) production point heat flux after 2000d ${Q_T}^{2000d}$ (Wm^{-2}), (**h**) production point heat flux after 10,000 days ${Q_T}^{10000d}$ (Wm^{-2}) and (**i**) time of 80% reach $T_{80\%}$ (**d**).

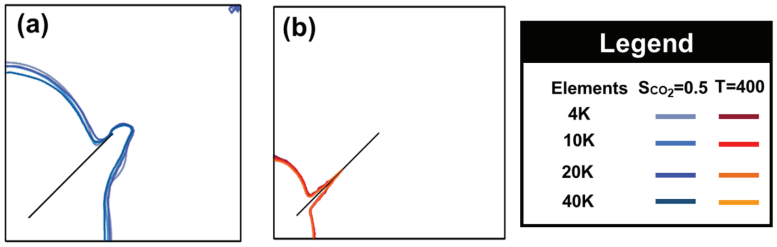


Figure A2: Spatial representation of carbon dioxide saturation and temperature in function of certain mesh number: (**a**) 50% carbon dioxide saturation contourlines for approximately 4000, 10,000, 20,000 and 40,000 elements and (**b**) 400K (127°C) temperature contourlines for approximately 4000, 10,000, 20,000 and 40,000 elements.

Appendix B

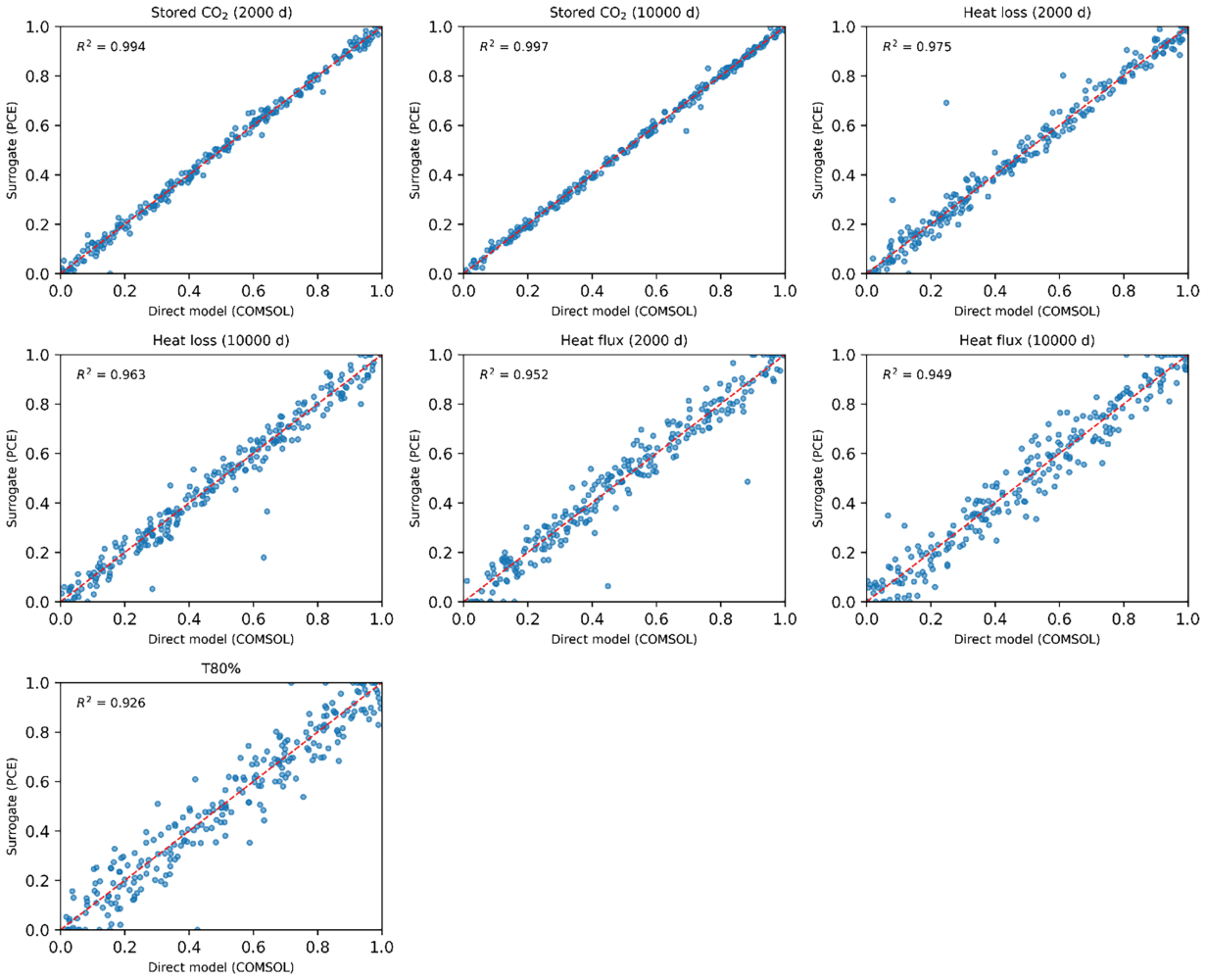


Figure A3: The comparative results of PCE-vs-COMSOL for the seven metrics (normalized).

References

1. Randolph JB, Saar MO. Coupling carbon dioxide sequestration with geothermal energy capture in naturally permeable, porous geologic formations: implications for CO_2 sequestration. Energy Proc. 2011;4:2206–13. doi:10.1016/j.egypro.2011.02.108.
2. Hawkes CD, McLellan PJ, Zimmer U, Bachu S. Geomechanical factors affecting geological storage of CO_2 in depleted oil and gas reservoirs. In: Proceedings of the Canadian International Petroleum Conference; 2004 Jun 8–10; Calgary, Alberta. p. PETSOC-2004-258. doi:10.2118/2004-258.
3. Rajabi MM, Chen M, Bozorgpour A, Al-Maktoumi A, Izady A. Stochastic techno-economic analysis of CO_2-circulated geothermal energy production in a closed reservoir system. Geothermics. 2021;96(2):102202. doi:10.1016/j.geothermics.2021.102202.
4. Roefs P, Moretti M, Welkenhuysen K, Piessens K, Compernolle T. CO_2-enhanced oil recovery and CO_2 capture and storage: an environmental economic trade-off analysis. J Environ Manag. 2019;239(5):167–77. doi:10.1016/j.jenvman.2019.03.007.
5. Cao C, Liao J, Hou Z, Wang G, Feng W, Fang Y. Parametric uncertainty analysis for CO_2 sequestration based on distance correlation and support vector regression. J Nat Gas Sci Eng. 2020;77(1):103237. doi:10.1016/j.jngse.2020.103237.
6. Sun F, Yao Y, Li G, Li X. Performance of geothermal energy extraction in a horizontal well by using CO_2 as the working fluid. Energy Convers Manag. 2018;171(7):1529–39. doi:10.1016/j.enconman.2018.06.092.
7. Dai Z, Viswanathan H, Xiao T, Middleton R, Pan F, Ampomah W, et al. CO_2 sequestration and enhanced oil recovery at depleted oil/gas reservoirs. Energy Proc. 2017;114:6957–67. doi:10.1016/j.egypro.2017.08.034.
8. Ganjdanesh R, Bryant SL, Orbach R, Pope GA, Sepehrnoori K. Coupled CO_2 sequestration and energy production from geopressured-geothermal aquifers. In: Proceedings of the Carbon Management Technology Conference; 2012 Feb 7–9; Orlando, FL, USA. p. CMTC-151351-MS. doi:10.7122/151351-ms.
9. Adams B, Saar MO, Bielicki JM, Ogland-Hand JD, Fleming MR. Using geologically sequestered CO_2 to generate and store geothermal electricity: CO_2 plume geothermal (CPG). In: Proceedings of the 2nd Applied Energy Symposium: MIT A+ B (MITAB 2020); 2020 Aug 13; Cambridge, MA, USA. p. APEN-MIT.
10. Cao C, Liu H, Hou Z, Mehmood F, Liao J, Feng W. A review of CO_2 storage in view of safety and cost-effectiveness. Energies. 2020;13(3):600. doi:10.3390/en13030600.
11. Chen M, Al-Maktoumi A, Mahdi Rajabi M, Izady A, Al-Mamari H, Cai J. Evaluation of CO_2 sequestration and circulation in fault-bounded thin geothermal reservoirs in North *Oman* using response surface methods. J Hydrol. 2021;598(4):126411. doi:10.1016/j.jhydrol.2021.126411.
12. Chen M, Al-Saidi A, Al-Maktoumi A, Izady A. The impact of geological heterogeneity on horizontal well-triplet performance in CO_2-circulated geothermal reservoirs. Adv Geo-Energy Res. 2022;6(3):192–205. doi:10.46690/ager.2022.03.03.
13. Ezekiel J, Adams BM, Saar MO, Ebigbo A. Numerical analysis and optimization of the performance of CO_2-plume geothermal (CPG) production wells and implications for electric power generation. Geothermics. 2022;98:102270. doi:10.1016/j.geothermics.2021.102270.
14. Abe A, Tamura K, Hirase K, Terai A, Tosha T. Numerical study on thermal performance of enhanced geothermal system with CO_2 using multistage hydraulic stimulation. Sustain Energy Res. 2025;12(1):40. doi:10.1186/s40807-025-00189-5.
15. Gudala M, Tariq Z, Govindarajan SK, Yan B, Sun S. Fractured geothermal reservoir using CO_2 as geofluid: numerical analysis and machine learning modeling. ACS Omega. 2024;9(7):7746–69. doi:10.1021/acsomega.3c07215.
16. Jeanne P, Guglielmi Y, Cappa F. Dissimilar properties within a carbonate-reservoir's small fault zone, and their impact on the pressurization and leakage associated with CO_2 injection. J Struct Geol. 2013;47(4):25–35. doi:10.1016/j.jsg.2012.10.010.
17. Li S, Zhang Y, Zhang X. A study of conceptual model uncertainty in large-scale CO_2 storage simulation. Water Resour Res. 2011;47(5):2010WR009707. doi:10.1029/2010WR009707.

18. Lie KA, Nilsen HM, Andersen O, Møyner O. A simulation workflow for large-scale CO_2 storage in the Norwegian North Sea. Comput Geosci. 2016;20(3):607–22. doi:10.1007/s10596-015-9487-6.
19. March R, Doster F, Geiger S. Assessment of CO_2 storage potential in naturally fractured reservoirs with dual-porosity models. Water Resour Res. 2018;54(3):1650–68. doi:10.1002/2017WR022159.
20. Middleton RS, Keating GN, Stauffer PH, Jordan AB, Viswanathan HS, Kang QJ, et al. The cross-scale science of CO_2 capture and storage: from pore scale to regional scale. Energy Environ Sci. 2012;5(6):7328. doi:10.1039/c2ee03227a.
21. Mogensen K, Masalmeh S. A review of EOR techniques for carbonate reservoirs in challenging geological settings. J Petrol Sci Eng. 2020;195(4):107889. doi:10.1016/j.petrol.2020.107889.
22. Trivedi J, Babadagli T. Efficiency analysis of greenhouse gas sequestration during miscible CO_2 injection in fractured oil reservoirs. Environ Sci Technol. 2008;42(15):5473–9. doi:10.1021/es703264r.
23. Zhang K, Jia N, Liu L. CO_2 storage in fractured nanopores underground: phase behaviour study. Appl Energy. 2019;238:911–28. doi:10.1016/j.apenergy.2019.01.088.
24. Burchette TP. Carbonate rocks and petroleum reservoirs: a geological perspective from the industry. Geol Soc Lond Spec Publ. 2012;370(1):17–37. doi:10.1144/sp370.14.
25. Bakhshi E, Torab FM. Determining wettability of fractured carbonate reservoirs. Nat Resour Res. 2016;25(2):211–25. doi:10.1007/s11053-015-9282-z.
26. Bachu S, Shaw J. Evaluation of the CO_2 sequestration capacity in Alberta's oil and gas reservoirs at depletion and the effect of underlying aquifers. J Can Petrol Technol. 2003;42(9):PETSOC-03-09-02. doi:10.2118/03-09-02.
27. Liu X, Falcone G, Alimonti C. A systematic study of harnessing low-temperature geothermal energy from oil and gas reservoirs. Energy. 2018;142:346–55. doi:10.1016/j.energy.2017.10.058.
28. Yan M, Ai C, Fu X, Zhang J, Han X, Cong Z, et al. Numerical modeling study on mineral alteration and sealing performance for CO_2 geological sequestration with enhancing water recovery in hydraulic fractured shale reservoirs. Lithosphere. 2021;2021(Special 4):7265408. doi:10.2113/2021/7265408.
29. Onoja MU, Shariatipour SM. The impact of gradational contact at the reservoir-seal interface on geological CO_2 storage capacity and security. Int J Greenh Gas Control. 2018;72(5):1–13. doi:10.1016/j.ijggc.2018.03.007.
30. Wang X, Jardani A, Jourde H, Lonergan L, Cosgrove J, Gosselin O, et al. Characterisation of the transmissivity field of a fractured and karstic aquifer, Southern France. Adv Water Resour. 2016;87(12):106–21. doi:10.1016/j.advwatres.2015.10.014.
31. Berkowitz B. Characterizing flow and transport in fractured geological media: a review. Adv Water Resour. 2002;25(8–12):861–84. doi:10.1016/S0309-1708(02)00042-8.
32. Bachu S, Adams JJ. Sequestration of CO_2 in geological media in response to climate change: capacity of deep saline aquifers to sequester CO_2 in solution. Energy Convers Manag. 2003;44(20):3151–75. doi:10.1016/S0196-8904(03)00101-8.
33. Wang Z, Li H, Liu S, Xu J, Liu J, Wang X. Risk evaluation of CO_2 leakage through fracture zone in geological storage reservoir. Fuel. 2023;342(2):127896. doi:10.1016/j.fuel.2023.127896.
34. Hui G, Chen Z, Schultz R, Chen S, Song Z, Zhang Z, et al. Intricate unconventional fracture networks provide fluid diffusion pathways to reactivate pre-existing faults in unconventional reservoirs. Energy. 2023;282:128803. doi:10.1016/j.energy.2023.128803.
35. Alanazi A, Baban A, Ali M, Keshavarz A, Iglauer S, Hoteit H. Residual trapping of CO_2, N_2, and a CO_2-N_2 mixture in *Indiana limestone* using robust NMR coreflooding: implications for CO_2 geological storage. Fuel. 2023;353(5):129221. doi:10.1016/j.fuel.2023.129221.
36. Sori A, Moghaddas J, Abedpour H. Comprehensive review of experimental studies, numerical modeling, leakage risk assessment, monitoring, and control in geological storage of carbon dioxide: implications for effective CO_2 deployment strategies. Greenh Gases Sci Technol. 2024;14(5):887–913. doi:10.1002/ghg.2295.
37. Viswanathan HS, Ajo-Franklin J, Birkholzer JT, Carey JW, Guglielmi Y, Hyman JD, et al. From fluid flow to coupled processes in fractured rock: recent advances and new frontiers. Rev Geophys. 2022;60(1):e2021RG000744. doi:10.1029/2021rg000744.

38. Chen M, Al-Maktoumi A, Izady A, Cai J, Dong Y. Use closed reservoirs for CO_2 storage and heat recovery: a two-stage brine-extraction and CO_2-circulation strategy. Sustain Energy Technol Assess. 2022;52(2):102346. doi:10.1016/j.seta.2022.102346.
39. Wang YZ, Cao RY, Jia ZH, Wang BY, Ma M, Cheng LS. A multi-mechanism numerical simulation model for CO_2-EOR and storage in fractured shale oil reservoirs. Petrol Sci. 2024;21(3):1814–28. doi:10.1016/j.petsci.2024.02.006.
40. Ma T, Jiang L, Liu Y, Guo C, Shen W, Xu Y. Numerical simulation of CO_2-enhanced oil recovery in fractured shale reservoirs using discontinuous and continuous Galerkin finite element methods. Front Energy Res. 2024;11:1330290. doi:10.3389/fenrg.2023.1330290.
41. Li Y, Zhu Y, Li Z, Jiang T, Xue Z, Shen Z, et al. Shale oil recovery by CO_2 injection in Jiyang Depression, Bohai Bay Basin, East China. Petrol Explor Dev. 2024;51(4):981–92. doi:10.1016/S1876-3804(24)60519-7.
42. Zhu Z, Song Y, Gao Q, Wang C. The application of CO_2-responsive materials on enhanced oil recovery for fractured tight oil reservoirs. Front Earth Sci. 2023;10:1053307. doi:10.3389/feart.2022.1053307.
43. Junji Yamaguchi A, Sato T, Tobase T, Wei X, Huang L, Zhang J, et al. Multiscale numerical simulation of CO_2 hydrate storage using machine learning. Fuel. 2023;334(B10):126678. doi:10.1016/j.fuel.2022.126678.
44. Guo Y, Li S, Sun H, Wu D, Liu L, Zhang N, et al. Enhancing gas production and CO_2 sequestration from marine hydrate reservoirs through optimized CO_2 hydrate cap. Energy. 2024;303(2):131821. doi:10.1016/j.energy.2024.131821.
45. Mahmoodpour S, Singh M, Mahyapour R, Omrani S, Sass I. Numerical simulation of carbon dioxide–nitrogen mixture dissolution in water-saturated porous media: considering cross-diffusion effects. Fluids. 2023;8(1):22. doi:10.3390/fluids8010022.
46. Di C, Wei Y, Wang K, Liu B, Deng P, Sun Z, et al. A parallel compositional reservoir simulator for large-scale CO_2 geological storage modeling and assessment. Sci Total Environ. 2024;955(81):177065. doi:10.1016/j.scitotenv.2024.177065.
47. Bui QM, Hamon FP, Castelletto N, Osei-Kuffuor D, Settgast RR, White JA. Multigrid reduction preconditioning framework for coupled processes in porous and fractured media. Comput Meth Appl Mech Eng. 2021;387(4):114111. doi:10.1016/j.cma.2021.114111.
48. Chen B, Harp DR, Lin Y, Keating EH, Pawar RJ. Geologic CO_2 sequestration monitoring design: a machine learning and uncertainty quantification based approach. Appl Energy. 2018;225(4):332–45. doi:10.1016/j.apenergy.2018.05.044.
49. Chen B, Harp DR, Lu Z, Pawar RJ. Reducing uncertainty in geologic CO_2 sequestration risk assessment by assimilating monitoring data. Int J Greenh Gas Control. 2020;94(3):102926. doi:10.1016/j.ijggc.2019.102926.
50. Smith RC. Uncertainty quantification: theory, implementation, and applications. Philadelphia, PA, USA: Society for Industrial and Applied Mathematics; 2013. doi:10.1137/1.9781611973228.
51. Xiao T, Chen T, Ma Z, Tian H, Meguerdijian S, Chen B, et al. A review of risk and uncertainty assessment for geologic carbon storage. Renew Sustain Energy Rev. 2024;189(80):113945. doi:10.1016/j.rser.2023.113945.
52. Babaei M. Integrated carbon sequestration–geothermal heat recovery: performance comparison between open and close systems. Transp Porous Medium. 2019;126(1):249–73. doi:10.1007/s11242-018-1042-1.
53. Sun Y, Tong C, Trainor-Guitton WJ, Lu C, Mansoor K, Carroll SA. Global sampling for integrating physics-specific subsystems and quantifying uncertainties of CO_2 geological sequestration. Int J Greenh Gas Control. 2013;12(1):108–23. doi:10.1016/j.ijggc.2012.10.004.
54. Dai Z, Viswanathan H, Middleton R, Pan F, Ampomah W, Yang C, et al. CO_2 accounting and risk analysis for CO_2 sequestration at enhanced oil recovery sites. Environ Sci Technol. 2016;50(14):7546–54. doi:10.1021/acs.est.6b01744.
55. Gan M, Nguyen MC, Zhang L, Wei N, Li J, Lei H, et al. Impact of reservoir parameters and wellbore permeability uncertainties on CO_2 and brine leakage potential at the Shenhua CO_2 Storage Site, China. Int J Greenh Gas Control. 2021;111(12):103443. doi:10.1016/j.ijggc.2021.103443.

56. Song Y, Sung W, Jang Y, Jung W. Application of an artificial neural network in predicting the effectiveness of trapping mechanisms on CO_2 sequestration in saline aquifers. Int J Greenh Gas Control. 2020;98(14–15):103042. doi:10.1016/j.ijggc.2020.103042.
57. Jia W, McPherson B, Pan F, Dai Z, Xiao T. Uncertainty quantification of CO_2 storage using Bayesian model averaging and polynomial chaos expansion. Int J Greenh Gas Control. 2018;71(10):104–15. doi:10.1016/j.ijggc.2018.02.015.
58. Sahu Q, Fahs M, Hoteit H. Optimization and uncertainty quantification method for reservoir stimulation through carbonate acidizing. ACS Omega. 2022;8(1):539–54. doi:10.1021/acsomega.2c05564.
59. Alqahtani A, He X, Yan B, Hoteit H. Uncertainty analysis of CO_2 storage in deep saline aquifers using machine learning and Bayesian optimization. Energies. 2023;16(4):1684. doi:10.3390/en16041684.
60. Shi H, Li J, Shen H, Li X, Wei N, Wang Y, et al. Quantitative analysis of the numerical simulation uncertainties from geological models in CO_2 geological storage: a case study of Shenhua CCS project. Int J Greenh Gas Control. 2024;135:104142. doi:10.1016/j.ijggc.2024.104142.
61. Wainwright HM, Finsterle S, Zhou Q, Birkholzer JT. Modeling the performance of large-scale CO_2 storage systems: a comparison of different sensitivity analysis methods. Int J Greenh Gas Control. 2013;17(1):189–205. doi:10.1016/j.ijggc.2013.05.007.
62. Rosolem R, Gupta HV, Shuttleworth WJ, Zeng X, de Gonçalves LGG. A fully multiple-criteria implementation of the Sobol' method for parameter sensitivity analysis. J Geophys Res Atmos. 2012;117(D7):2011JD016355. doi:10.1029/2011JD016355.
63. Li C, Mahadevan S. An efficient modularized sample-based method to estimate the first-order Sobol? Index. Reliab Eng Syst Saf. 2016;153:110–21. doi:10.1016/j.ress.2016.04.012.
64. Birkholzer JT, Zhou Q, Cortis A, Finsterle S. A sensitivity study on regional pressure buildup from large-scale CO_2 storage projects. Energy Proc. 2011;4(4):4371–8. doi:10.1016/j.egypro.2011.02.389.
65. Dai Z, Middleton R, Viswanathan H, Fessenden-Rahn J, Bauman J, Pawar R, et al. An integrated framework for optimizing CO_2 sequestration and enhanced oil recovery. Environ Sci Technol Lett. 2014;1(1):49–54. doi:10.1021/ez4001033.
66. Saad BM, Alexanderian A, Prudhomme S, Knio OM. Probabilistic modeling and global sensitivity analysis for CO_2 storage in geological formations: a spectral approach. Appl Math Model. 2018;53(4):584–601. doi:10.1016/j.apm.2017.09.016.
67. Chiaramonte L, White JA, Trainor-Guitton W. Probabilistic geomechanical analysis of compartmentalization at the Snøhvit CO_2 sequestration project. J Geophys Res Solid Earth. 2015;120(2):1195–209. doi:10.1002/2014JB011376.
68. Ren J, Feng D. Sensitivity analysis strategy to assess the salting-out problem during CO_2 geological storage process. Shock Vib. 2021;2021(1):2809467. doi:10.1155/2021/2809467.
69. Onishi T, Nguyen MC, Carey JW, Will B, Zaluski W, Bowen DW, et al. Potential CO_2 and brine leakage through wellbore pathways for geologic CO_2 sequestration using the national risk assessment partnership tools: application to the big sky regional partnership. Int J Greenh Gas Control. 2019;81(3):44–65. doi:10.1016/j.ijggc.2018.12.002.
70. Baisch S, Weidler R, Voros R, Wyborn D, de Graaf L. Induced seismicity during the stimulation of a geothermal HFR reservoir in the Cooper Basin, Australia. Bull Seismol Soc Am. 2006;96(6):2242–56. doi:10.1785/0120050255.
71. Brown DW. Hot dry rock geothermal energy: important lessons from Fenton Hill. In: Proceedings of the Thirty-Fourth Workshop on Geothermal Reservoir Engineering; 2009 Feb 9–11; Stanford, CA, USA. p. SGP-TR-187.
72. Llanos EM, Zarrouk SJ, Hogarth RA. Numerical model of the Habanero geothermal reservoir, Australia. Geothermics. 2015;53:308–19. doi:10.1016/j.geothermics.2014.07.008.
73. Genter A, Cuenot N, Melchert B, Moeckes W, Ravier G, Sanjuan B, et al. Main achievements from the multi-well EGS Soultz project during geothermal exploitation from 2010 and 2012. In: Proceedings of European Geothermal Congress 2013; 2013 Jun 12; Pise, Italy. p. al-00812959.
74. Guo B, Fu P, Hao Y, Peters CA, Carrigan CR. Thermal drawdown-induced flow channeling in a single fracture in EGS. Geothermics. 2016;61(2):46–62. doi:10.1016/j.geothermics.2016.01.004.
75. Bear J. Dynamics of fluids in porous media. Soil Sci. 1975;120(2):162–3. doi:10.1097/00010694-197508000-00022.

76. Kolditz O, Shao H, Wang W, Bauer S. Thermo-hydro-mechanical chemical processes in fractured porous media: modelling and benchmarking. Berlin/Heidelberg, Germany: Springer; 2016.
77. van Genuchten MT. A closed-form equation for predicting the hydraulic conductivity of unsaturated soils. Soil Sci Soc Am J. 1980;44(5):892–8. doi:10.2136/sssaj1980.03615995004400050002x.
78. Mualem Y. A new model for predicting the hydraulic conductivity of unsaturated porous media. Water Resour Res. 1976;12(3):513–22. doi:10.1029/WR012i003p00513.
79. Koohbor B, Fahs M, Ataie-Ashtiani B, Belfort B, Simmons CT, Younes A. Uncertainty analysis for seawater intrusion in fractured coastal aquifers: effects of fracture location, aperture, density and hydrodynamic parameters. J Hydrol. 2019;571(SP479):159–77. doi:10.1016/j.jhydrol.2019.01.052.
80. Koohbor B, Fahs M, Hoteit H, Doummar J, Younes A, Belfort B. An advanced discrete fracture model for variably saturated flow in fractured porous media. Adv Water Resour. 2020;140:103602. doi:10.1016/j.advwatres.2020.103602.
81. Koohbor B, Deparis J, Leroy P, Ataie-Ashtiani B, Davarzani H, Colombano S. DNAPL flow and complex electrical resistivity evolution in saturated porous media: a coupled numerical simulation. J Contam Hydrol. 2022;248(3):104003. doi:10.1016/j.jconhyd.2022.104003.
82. Lu H, Saló-Salgado L, Marzouk YM, Juanes R. Uncertainty quantification of fluid leakage and fault instability in geologic CO_2 storage. Water Resour Res. 2025;61(10):e2024WR039275. doi:10.1029/2024WR039275.
83. Pruess K. On production behavior of enhanced geothermal systems with CO_2 as working fluid. Energy Convers Manag. 2008;49(6):1446–54. doi:10.1016/j.enconman.2007.12.029.
84. Xu T, Feng G, Hou Z, Tian H, Shi Y, Lei H. Wellbore–reservoir coupled simulation to study thermal and fluid processes in a CO_2-based geothermal system: identifying favorable and unfavorable conditions in comparison with water. Environ Earth Sci. 2015;73(11):6797–813. doi:10.1007/s12665-015-4293-y.
85. Li L, Voskov D. A novel hybrid model for multiphase flow in complex multi-scale fractured systems. J Petrol Sci Eng. 2021;203(5):108657. doi:10.1016/j.petrol.2021.108657.
86. Sobol' M. Global sensitivity indices for nonlinear mathematical models and their Monte Carlo estimates. Math Comput Simul. 2001;55(1–3):271–80. doi:10.1016/S0378-4754(00)00270-6.
87. Rajabi MM, Fahs M, Panjehfouladgaran A, Ataie-Ashtiani B, Simmons CT, Belfort B. Uncertainty quantification and global sensitivity analysis of double-diffusive natural convection in a porous enclosure. Int J Heat Mass Transf. 2020;162(6):120291. doi:10.1016/j.ijheatmasstransfer.2020.120291.
88. Herman J, Usher W. SALib: an open-source Python library for sensitivity analysis. J Open Source Softw. 2017;2(9):97. doi:10.21105/joss.00097.
89. Qian E, Peherstorfer B, O'Malley D, Vesselinov VV, Willcox K. Multifidelity Monte Carlo estimation of variance and sensitivity indices. ASA J Uncertain Quantif. 2018;6(2):683–706. doi:10.1137/17m1151006.
90. Fajraoui N, Fahs M, Younes A, Sudret B. Analyzing natural convection in porous enclosure with polynomial chaos expansions: effect of thermal dispersion, anisotropic permeability and heterogeneity. Int J Heat Mass Transf. 2017;115(8):205–24. doi:10.1016/j.ijheatmasstransfer.2017.07.003.
91. Li H, Zhang D. Probabilistic collocation method for flow in porous media: comparisons with other stochastic methods. Water Resour Res. 2007;43(9):2006WR005673. doi:10.1029/2006WR005673.
92. Oladyshkin S, Nowak W. Data-driven uncertainty quantification using the arbitrary polynomial chaos expansion. Reliab Eng Syst Saf. 2012;106(1):179–90. doi:10.1016/j.ress.2012.05.002.
93. Feinberg J, Langtangen HP. Chaospy: an open source tool for designing methods of uncertainty quantification. J Comput Sci. 2015;11(9):46–57. doi:10.1016/j.jocs.2015.08.008.
94. McKenna SA, Walker DD, Arnold B. Modeling dispersion in three-dimensional heterogeneous fractured media at *Yucca* Mountain. J Contam Hydrol. 2003;62–63(9):577–94. doi:10.1016/s0169-7722(02)00189-4.
95. Geiger S, Cortis A, Birkholzer JT. Upscaling solute transport in naturally fractured porous media with the continuous time random walk method. Water Resour Res. 2010;46(12):2010WR009133. doi:10.1029/2010WR009133.
96. Wang N, Chang H, Zhang D. Efficient uncertainty quantification for dynamic subsurface flow with surrogate by theory-guided neural network. Comput Meth Appl Mech Eng. 2021;373(9):113492. doi:10.1016/j.cma.2020.113492.

97. Tang M, Ju X, Durlofsky LJ. Deep-learning-based coupled flow-geomechanics surrogate model for CO_2 sequestration. Int J Greenh Gas Control. 2022;118(10):103692. doi:10.1016/j.ijggc.2022.103692.
98. Sun Z, Salazar-Tio R, Wu L, Bostrøm B, Fager A, Crouse B. Geomechanical assessment of a large-scale CO_2 storage and insights from uncertainty analysis. Geoenergy Sci Eng. 2023;224:211596. doi:10.1016/j.geoen.2023.211596.
99. Seabra GS, Mücke NT, Santos Silva VL, Voskov D, Vossepoel FC. AI enhanced data assimilation and uncertainty quantification applied to geological carbon storage. Int J Greenh Gas Control. 2024;136(2194):104190. doi:10.1016/j.ijggc.2024.104190.